Wang *et al. Energy Mater.* **2025**, *5*, 500022
DOI: 10.20517/energymater.2024.102

Energy Materials

Article

Open Access

Check for updates

Understanding Mg-ion deposition behavior on MgBi alloy in solid-state form

Qian Wang[1,2], Hao Li[3], Ting Xu[1], Yungui Chen[1,4], Yigang Yan[1,4,*]

[1]Institute of New Energy and Low-Carbon Technology, Sichuan University, Chengdu 610207, Sichuan, China.
[2]College of Materials Science and Engineering, Sichuan University, Chengdu 610065, Sichuan, China.
[3]Advanced Institute for Materials Research (AIMR), Tohoku University, Sendai 980-8577, Japan.
[4]Engineering Research Center of Alternative Energy Materials and Devices, Ministry of Education, Sichuan University, Chengdu 610065, Sichuan, China.

[*]**Correspondence to:** Prof. Yigang Yan, Institute of New Energy and Low-Carbon Technology, Sichuan University, Chuanda Road, Shuangliu Distinct, Chengdu 610207, Sichuan, China. E-mail: yigang.yan@scu.edu.cn

How to cite this article: Wang, Q.; Li, H.; Xu, T.; Chen, Y.; Yan, Y. Understanding Mg-ion deposition behavior on MgBi alloy in solid-state form. *Energy Mater.* **2025**, *5*, 500022. https://dx.doi.org/10.20517/energymater.2024.102

Received: 1 Aug 2024 **First Decision:** 27 Sep 2024 **Revised:** 23 Oct 2024 **Accepted:** 25 Nov 2024 **Published:** 13 Jan 2025

Academic Editor: Yuping Wu **Copy Editor:** Ping Zhang **Production Editor:** Ping Zhang

Abstract

Mg alloys have frequently been studied as anodes for Mg-ion batteries due to their high specific capacity and low electrochemical potential. In the present study, we investigated the interfacial stability of MgBi alloy anodes with solid-state electrolytes. The bubble-like solid electrolyte interface (SEI) was observed between the MgBi alloy anode and $Mg(BH_4)_2{\cdot}1.9NH_3$ solid-state electrolyte, leading to the unstable Mg stripping/plating on the MgBi alloy. Theoretical simulations suggest that the bubble-like SEI originates from the different Mg-ion dynamics on the eutectic region (e.g., Mg + Mg_3Bi_2 phases) and the Mg matrix. The addition of $MgBr_2{\cdot}2NH_3$ nanoparticles in $Mg(BH_4)_2{\cdot}1.9NH_3$ suppresses the formation of a bubble-like SEI through the etching effect of Br^- ions. Consequently, interfacial resistance is lowered and the interfacial stability is drastically enhanced, e.g., Mg stripping/plating for over 1,200 cycles at 0.1 mA cm^{-2} with a low overpotential around 0.05 V.

Keywords: MgBi alloy anode, solid-state electrolyte, Mg-ion battery, interfacial stability

INTRODUCTION

As one of the most abundant elements globally, constituting approximately 2.3 wt.% of the Earth's crust, magnesium (Mg) is recognized for its low-cost material benefits, possessing superior properties compared

to lithium. The development of Mg-ion batteries (MIBs), especially the batteries in the solid-state form, is limited by the slow Mg^{2+} migration both in the solid electrolyte and electrode[1]. Recently, great progress has been made in $Mg(BH_4)_2$-based materials as solid-state electrolytes (SSEs). By substituting$[BH_4]^-$ with other anions {e.g., $[NH_2]^-$[2-5]} or introducing neutral molecules [e.g., $NH_2(CH_2)_2NH_2$[6], diglyme[7], NH_3BH_3[8] and NH_3[9,10]], the $[BH_4]$ tetrahedral cages that confine the Mg^{2+} cations can be disrupted leading to significant improvement in Mg^{2+} conductivity. Further, the addition of metal oxide nanoparticles improves the ionic conductivity of $Mg(BH_4)_2{\cdot}xNH_3$ to 10^{-4} S cm^{-1} at room temperature[10-12], owing to the coordination-unlock effect of oxygen vacancies on the surface of metal oxide nanoparticles; the nanoparticles also show high reactivity[13]. However, the Mg metal anode is noted for its susceptibility to passivation and poor compatibility with electrolytes[14], decreasing the interfacial stability[15-17].

Electrolyte additives and the structure engineering of anodes have been chosen to eliminate the passivation effect. Combining with density functional theory (DFT) calculations and thermodynamic analysis, compounds such as $MgSiN_2$, MgSe, MgS, and MgX_2 (X = Cl, Br, and I) are identified as promising anode coating materials due to their reasonable Mg migration barriers[18]. The addition of both $MgCl_2$ and $MgBr_2$ results in the dissolution of the native passive layer and the formation of a passivating film that permits the diffusion of Mg^{2+}[17,19]. This behavior, associated with the reactivity of Cl^- anions, leads to homogeneous plating and stripping of Mg[19]. Impressively, our previous work reported that the *in situ* decoration of $MgBr_2{\cdot}2NH_3$ nanoparticles on the surface of $Mg(BH_4)_2{\cdot}1.9NH_3$ offers long-term interfacial stability towards the Mg metal anode[20]. The behavior of Br^- leads to the uniform Mg deposition on the surface of Mg metal similar to Cl^- anions in organic electrolytes.

However, it is crucial to highlight that in the Mg anode, only the α-Mg matrix phase is present[20], making it difficult to directly observe the formation of the passivation layer from the $Mg(BH_4)_2{\cdot}1.9NH_3$ electrolyte. Additionally, the corrosion process induced by Br^- ions in a single-phase Mg anode is particularly complex. The interaction between Br^- ions and the α-Mg surface can result in localized corrosion phenomena. This complexity is further heightened by the dynamic nature of the electrolyte interface, where passivation layer formation and corrosion occur simultaneously. The lack of structural diversity in the α-Mg phase restricts our ability to identify specific reaction pathways or transient states during solid electrolyte interface (SEI) formation. Addressing these challenges requires advanced characterization methods and a deeper understanding of the electrochemical mechanisms at play, particularly in the context of the $Mg(BH_4)_2{\cdot}1.9NH_3$-32 wt.% $MgBr_2{\cdot}2NH_3$ electrolyte.

To further investigate the corrosion behavior, a Mg alloy containing a second phase is ideal, especially for SSEs. In recent years, alloy anodes have gained significant attention due to their unique advantages and properties. Elements from groups IIIA, IVA, and VA (denoted as M) can theoretically form Mg_xM alloys with magnesium, offering high theoretical specific capacities at relatively low alloying potentials. Moreover, alloy materials can exhibit new properties that single metals do not possess, potentially creating synergistic effects that enhance magnesium storage performance. A variety of alloys (i.e., Mg_3Bi_2[21], Mg_2Sn[22,23], Mg_2Ga_5[24], and Mg-Sn-Bi@Mg[25]) have been reported as alternative anode materials for MIBs. Metallic gallium (Ga), due to its unique liquid state at room temperature, can prevent volume changes in the anode and provide long-term cycling stability in conventional electrolytes[24]. Tin (Sn) as an anode material offers a high theoretical capacity (903 mAh g^{-1}) and operates at a low voltage. During the alloying process, Sn^{2+} is reduced and deposits as metallic tin on the anode surface, breaking the passivation layer and promoting magnesium dissolution. However, during oxidation, the bulk Sn alloying process with Mg is slow and causes significant volume expansion. This leads to the formation of amorphous Mg_2Sn during subsequent de-magnesium processes, resulting in noticeable capacity decay[26].

In contrast to Sn, bismuth (Bi) exhibits higher reversibility as an anode material[27]. Theoretical calculations indicate that Mg-ion mobility in Bi anodes is higher than that of Li ions[28]. However, Bi is limited by lower theoretical specific capacity (384 mAh g^{-1}) and its (de)magnesiation occurs at a high voltage of 0.28 V (*vs.* Mg^{2+}/Mg)[29], which restricts its practical applicability. These challenges highlight the need for significant improvements and structural optimizations to enhance its performance. On the other hand, the rhombic crystal structure of Bi promotes the formation of alloys that offer a high-volume capacity (3,783 mA h cm^{-3}), comparable to that of Mg. Therefore, Bi is considered to be the best anode model for future studies of complete MIB systems[27]. Additionally, MgBi alloys circumvent the initial slow electrochemical alloying process between Mg and Bi, further enhancing their potential as anode materials.

In this work, we investigated the interfacial stability of a MgBi alloy anode with a SSE. For the first time, we observed the formation of a bubble-like SEI between MgBi and $Mg(BH_4)_2 \cdot 1.9NH_3$ electrolytes, which impedes the stable Mg stripping/ platting. The introduction of $MgBr_2 \cdot 2NH_3$ nanoparticles in the electrolyte could suppress the bubble-like SEI, enabling the long-term stable stripping/plating over 600 h at 0.1 mA cm^{-2}. The mechanism of formation and suppression of the bubble-like SEI were investigated by a combination of experimental analyses and theoretical calculations. These findings provide a comprehensive understanding of the interfacial stability of alloy anodes in solid-state form and are highly conducive to the development of efficient and durable solid-state MIBs.

EXPERIMENTAL

Material preparation

$Mg(BH_4)_2 \cdot 1.9NH_3$ (labeled as MBN) and $Mg(BH_4)_2 \cdot 1.9NH_3$-32 wt.% $MgBr_2 \cdot 2NH_3$ (labeled as MBN-Br) were synthesized according to the protocol described in the literature[20]. Metallic Mg (99.99%) and Mg20Bi alloys, composed of 80% Mg and 20% Bi, were repeatedly polished in an argon-filled glove box before use and then cut into 6mm diameter pieces for electrochemical measurements.

Structural characterization

X-ray diffraction (XRD) data were collected at room temperature using a Rigaku SmartLab diffractometer equipped with a rotating Cu anode (Cu Kα radiation, 2 kW, λ = 1.54056 Å). Before these analyses, the sheets were embedded in conductive cold-set resin and sanded to a 3,000-mesh finish, followed by mechanical polishing and etching. Due to the varying potentials between the phases in the alloy, each phase experiences different degrees of corrosion, leading to distinct microstructural features. The pristine MgBi alloy sheets were then etched using a solution composed of 10 g of oxalic acid in 100 mL of deionized (DI) water. The microstructure and element analyses of the alloy sheets were examined through optical microscopy (OM) and scanning electron microscopy (SEM). SEM analysis was conducted using SU-8200 equipped with an Oxford X-Max energy-dispersive X-ray spectrometer (EDS). The samples were loaded into a protective accessory and sealed in an argon atmosphere. The X-ray photograph spectroscopy (XPS) spectra were recorded on Thermo Scientific K-Alpha+, an XPS system. The spectra were corrected based on C 1*s* binding energy at 284.8 eV. Sub-surfaces of different depths were obtained by different argon ion etching times.

Electrochemical measurements

All pellets were prepared in an Ar-filled glovebox with a diameter of 6 mm and a thickness of ~1 mm under a pressure of 0.3 GPa and assembled in a Swagelok-type cell. Electrochemical impedance spectroscopy (EIS) and cyclic voltammetry (CV) tests were using the Multi Autolab M204 electrochemical workstation. A symmetric Mg (Mg20Bi) | MBN (MBN-Br) | Mg (Mg20Bi) cell was used for EIS test. The EIS measurements were conducted in a frequency range of 0.1 Hz to 1 MHz with an alternating current amplitude of 5 mV. An asymmetric Mg (Mg20Bi) | MBN | SS cell configuration was used for CV (scan rate of 10 mV s^{-1}). Galvanostatic cycling was conducted with a LANDCT2001A battery tester at 323 K. For the galvanostatic

cycling in the symmetric Mg (Mg20Bi) | MBN (MBN-Br) | Mg (Mg20Bi) cell.

Computational methods

DFT was performed with Vienna Ab-initio Simulation Package (VASP) 6.3[30]. Perdew-Burke-Ernzerhof (PBE) was utilized for exchange-correlation functional[31]. The wave functions were expanded in plane waves with a kinetic energy cutoff of 450 eV. We used Projector Augmented Wave (PAW) potentials to describe the interaction between the ions and electrons[32]. A Gaussian smearing of 0.02 eV for the Fermi-Dirac distribution function was used for calculations. The vacuum in the simulation box of interface geometry optimization is 15 Å. The lattice plane of an anode, identified from the XRD patterns, was considered as the substrate, e.g., (011) for Mg_3Bi_2 and (101) for Mg. The last two layers of substrate were fixed. Integration in the first Brillouin zone is performed using Monkhorst-Pack grids including 2 × 2 × 1 k-points for all interfaces[33]. The adsorption energies (E_{ads}) were calculated as $E_{ads} = E_{total} - (E_{anode} + E_{Mg})$, where the E_{total}, E_{anode}, and E_{Mg} represent the total energies of the Mg adsorption layer, anode layer, and the Mg atom, respectively. In all DFT calculations, the positions of the free atoms are optimized until the maximum force on any of them is less than 0.05 eV/Å. Convergence of energy differences for the used cutoff energies and k-point grids was ensured within a tolerance of 0.05 meV/atom. In the end, the climbing image nudged elastic band (CI-NEB) method[34] calculated Mg^{2+} migration on the surface of Mg and Mg_3Bi_2 with the convergence criterion set at 0.03 eV $Å^{-1}$.

RESULTS AND DISCUSSION

Figure 1 shows the microstructure and phase analysis results of the Mg20Bi binary alloy. The alloy contains two distinct phases: Mg matrix (black area) with surface area ranging from approximately 3,200 $μm^2$ (feature size: 80 μm) to 16,200 $μm^2$ (feature size: 180 μm) and the Mg_3Bi_2 phase (white area) as the grain boundaries, as shown in Figure 1A. The EDS mapping analysis in Figure 1B and C confirms the presence of Mg matrix surrounded by Bi-enriched regions. The proportion of the Mg_3Bi_2 phase in Mg20Bi alloys is estimated to be 13.5 wt.% based on the statistical results from OM in Supplementary Figure 1, which is consistent with the phase composition of the alloy[35]. As presented in Figure 1D, elemental composition analysis results indicate that the Mg matrix (Point 1 in Figure 1A) contains 96.7 wt.% Mg and 3.3 wt.% Bi, while the Mg_3Bi_2 phase (Point 2 in Figure 1A) contains 13.5 wt.% Mg and 86.5 wt.% Bi. The XRD pattern in Figure 1E indicates the presence of three phases in Mg20Bi alloys: 87.3 wt.% α-Mg, 9.1 wt.% Mg_3Bi_2 and 3.6 wt.% Bi_2O_3, as shown in Figure 1F. These results are consistent with the phase composition observed through OM [Supplementary Figure 1].

The electrochemical stability of Mg20Bi alloy anodes with MBN and MBN-Br is compared by CV measurements with a scanning rate of 10 mV s^{-1} at 50 °C, as illustrated in Supplementary Figure 2. The prominent oxidation peaks observed in both electrolytes indicate their compatibility with Mg20Bi alloys. Notably, a peak current density of 0.33 mA cm^{-2} observed for MBN-Br surpasses that for MBN electrolyte (0.002 mA cm^{-2}) by around 160 times, suggesting a much smaller interfacial resistance between Mg20Bi and MBN-Br.

The voltage profile of a symmetric cell, Mg20Bi | MBN-Br | Mg20Bi, at different current densities at 50 °C is shown in Supplementary Figure 3. Stable Mg^{2+} stripping/plating is initially observed at 0.5 mA cm^{-2}. The extended test of 1200 cycles over 600 h was performed at a current density of 0.1 mA cm^{-2} to assess the compatibility between the anode and electrolyte, as depicted in Figure 2A. The Mg20Bi | MBN | Mg20Bi symmetric cell shows significant polarization; *i.e.*, the overpotential continuously increases from an initial value of 0.18 V to 0.21 V at 100 h, 0.38 V at 300 h, and further to 0.57 V at 500 h. In contrast, the Mg20Bi | MBN-Br | Mg20Bi symmetric cell exhibits remarkably higher stability during the whole Mg

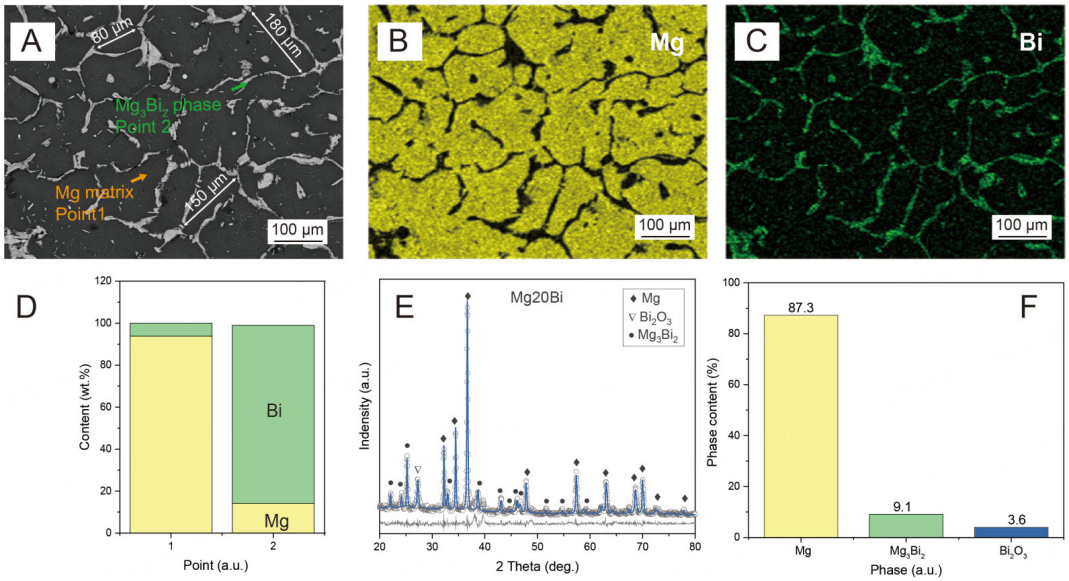

Figure 1. Structural characterization of Mg20Bi alloy. (A-C) SEM images and corresponding EDS mapping of Mg20Bi alloy; (D) EDS results for the two points indicated in Figure 1A. Mg and Bi elements are represented in yellow and green, respectively; (E) Rietveld refinement of XRD patterns for Mg20Bi, showing observed (grey circles) and calculated (line) curves, and a different curve below (grey line), R/E = 1.7; (F) The phase compositions. SEM: Scanning electron microscopy; EDS: Energy-dispersive X-ray spectrometer; XRD: X-ray diffraction.

stripping/plating, maintaining a notably low overpotential of 0.05 V over 600 h.

The variation of impedance during the Mg stripping/plating process of Mg20Bi | MBN | Mg20Bi and Mg20Bi | MBN-Br | Mg20Bi symmetric cells is recorded, as shown in Figure 2B and C, respectively. The EIS spectra of both symmetric cells, characterized by a semicircle as a typical feature of an ionic conductor, rule out the possibility of a short circuit, as shown in Supplementary Figure 4. The impedance of Mg20Bi | MBN | Mg20Bi cell displays a significant increase from 1 MΩ up to 20 MΩ over 600 h. In contrast, the impedance of the Mg20Bi | MBN-Br | Mg20Bi cell [Figure 2C] varies much more slightly, i.e., from an initial value of 1500 Ω to 1900 Ω at 600 h, which is consistent with the stable Mg stripping/plating behavior observed in the literature [Supplementary Table 1].

To understand the differences in impedance changes over the cycling time, the microstructure of the Mg20Bi alloy anode after cycling with MBN and MBN-Br is investigated. Figure 3A shows the surface morphology of Mg20Bi alloys before the cycling test, which is flat, with visible scratches resulting from sandpapering. After 600 h cycling in the Mg20Bi | MBN | Mg20Bi symmetric cell, as shown in Figure 3B, the surface of the Mg20Bi alloy comprises bubble-like grains with a surface area distribution between 3,200 μm^2 (feature size: 70 μm) and 9,900 μm^2 (feature size: 110 μm), which is similar to the surface area range of the initial alloy metallograph of the matrix Mg [Figure 1A]. Further, EDS mapping results in Figure 3C indicate that the bubble-like grains contain elements of Mg, B, and Bi. In particular, elements Mg and Bi are majorly distributed inside the bubble, whereas element B is concentrated at the edges of the bubble, suggesting that the edges of the bubble consist of electrolytes. The XRD pattern of the Mg20Bi alloy anode after 600 h of Mg stripping/plating is shown in Supplementary Figure 5. The peaks of Mg and Mg_3Bi_2 phases shift by approximately 0.32° toward lower angles, indicating lattice expansion due to Mg ion insertion.

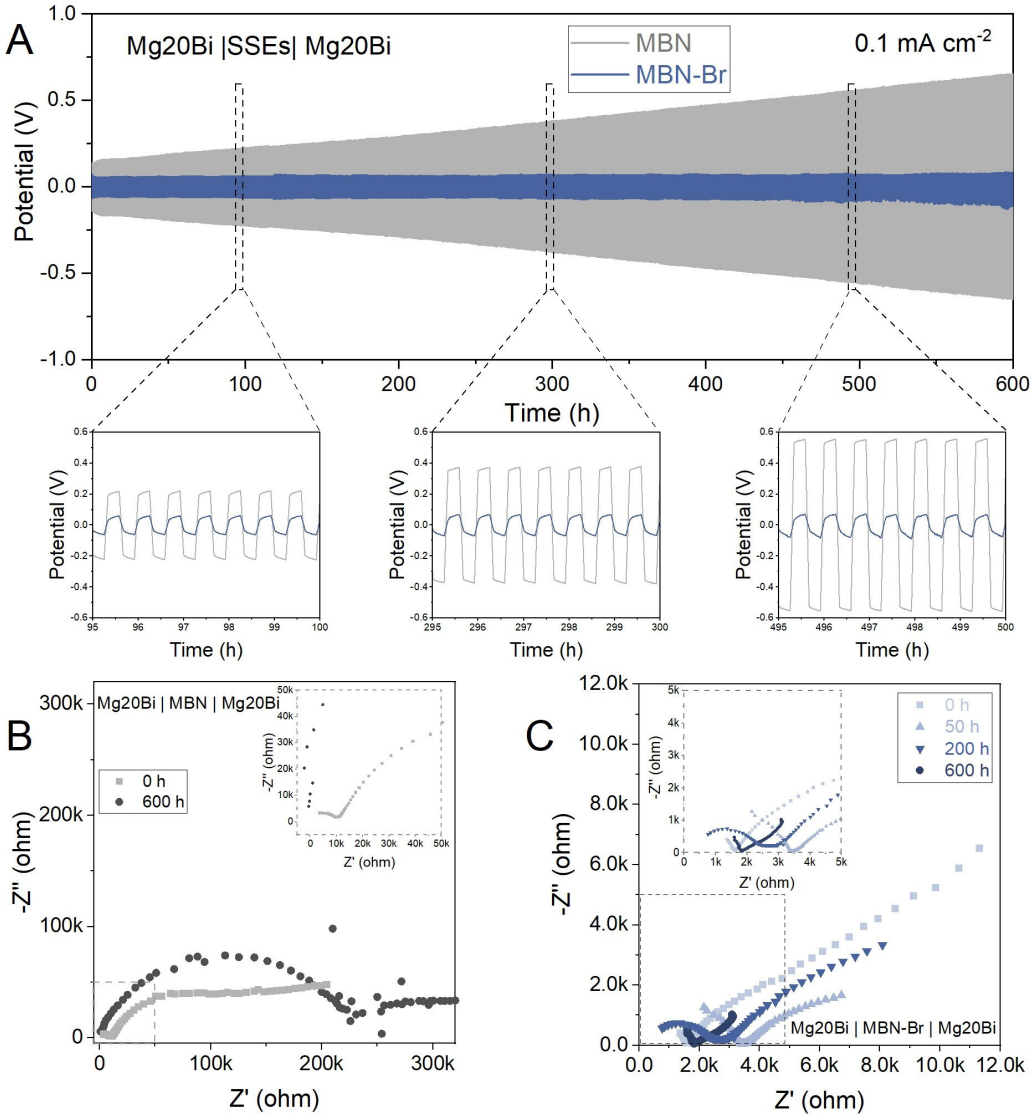

Figure 2. Electrochemical performance of Mg20Bi alloy anodes with different SSEs. (A) Long-term cycling curves of Mg20Bi alloy anodes with MBN and MBN-Br for a symmetric cell at 0.1 mA cm^{-2}.Enlargements show the detailed voltage plateau of Mg stripping/plating at a selected duration. Nyquist plots of the Mg20Bi | SSEs | Mg20Bi symmetric cell; SSEs (B) MBN and (C) MBN-Br. All measurements are conducted at T = 50 °C. SSEs: Solid-state electrolytes; MBN: $Mg(BH_4)_2{\cdot}1.9NH_3$; MBN-Br: $Mg(BH_4)_2{\cdot}1.9NH_3$-32 wt.% $MgBr_2{\cdot}2NH_3$.

Ex situ Mg 2*p* and Bi 4*f* XPS spectra are conducted to investigate the Mg and Bi chemical states at different etching times, as shown in Figure 3D. The peak of Mg 2*p* observed at 50.2 eV at an etching time of 0 s is assigned to Mg^{II}. At the same time, the doublet peaks of Bi $4f_{5/2}$ and Bi $4f_{7/2}$ appear around 163 eV and 158 eV, respectively. The Bi 4*f* doublet peaks at 0s confirm the presence of Bi^{III} and Bi^0, with the proportion of Bi^0 being 51.2%, relating to the metallic state from the Mg20Bi solid solution. The 48.8% Bi^{III} originates from intermetallic compounds formed by the newly deposited Mg with Bi, primarily leading to the formation of the intermetallic compound Mg_3Bi_2. When the etching time is increased to 150 s, the peak of Mg 2*p* blue-shifted to 49.9 eV, which is attributed to the reduced oxidation of Mg. The Bi 4*f* doublet peaks still indicate the presence of Bi^{III} and Bi^0, with the relative proportion of Bi^{III} decreasing to 9.1%, indicating a significant decrease in Mg_3Bi_2. With the etching time increased to 300 s, the Mg 2*p* peak and the Bi 4*f* peak

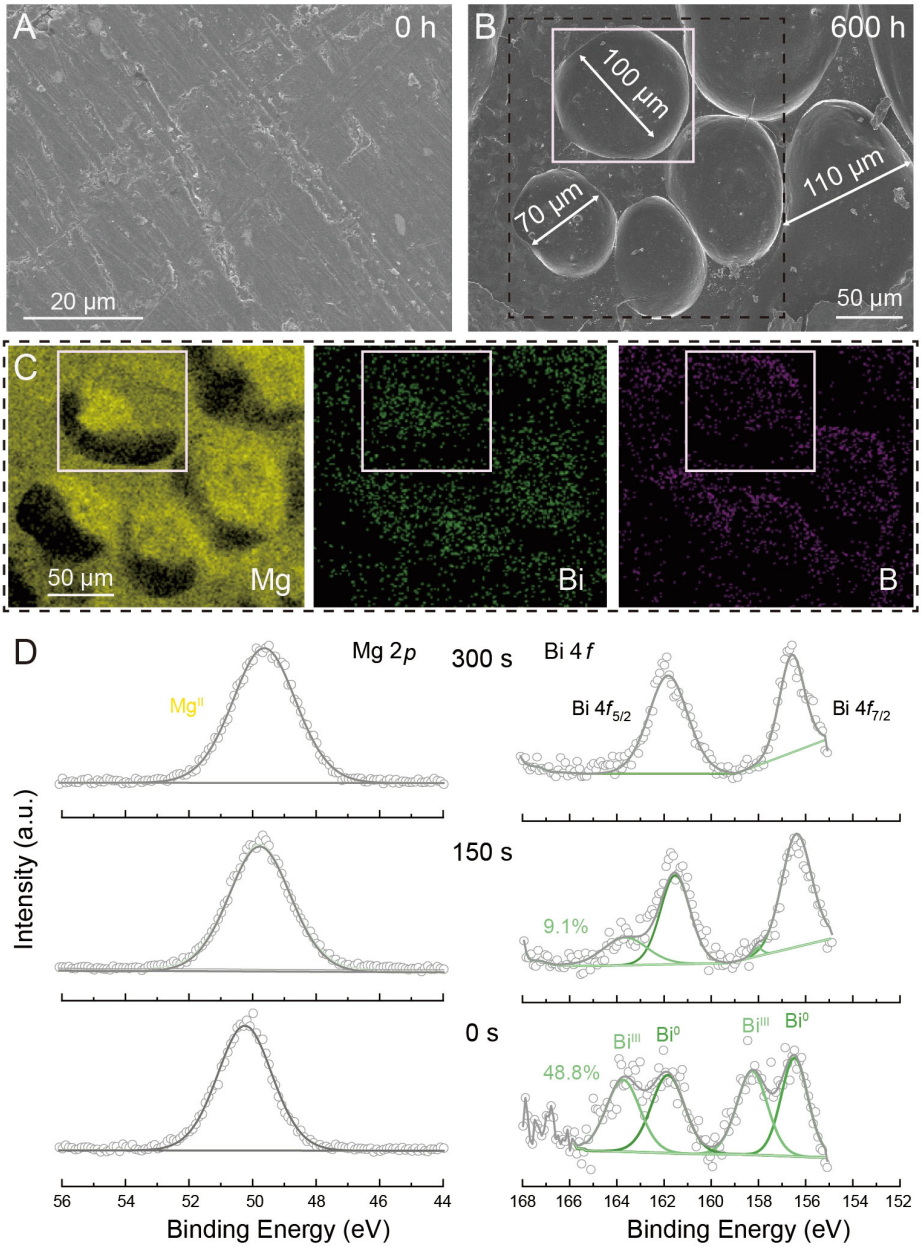

Figure 3. Mg20Bi alloy anode after cycling in Mg20Bi | MBN | Mg20Bi symmetric cell. SEM of Mg20Bi alloy anode: (A) 0 h and (B) after 600 h; (C) EDS mapping of the enlarged part in Figure 3B; (D) XPS spectra at different etching times: Mg 2*p* and Bi 4*f* in Mg20Bi alloy anode after 600 h stripping/plating. MBN: $Mg(BH_4)_2{\cdot}1.9NH_3$; SEM: Scanning electron microscopy; EDS: Energy-dispersive X-ray spectrometer; XPS: X-ray photograph spectroscopy.

only show the presence of a metallic state.

Combined with the SEM-EDS spectra, the Mg ion stripping/plating mechanism between the MBN electrolyte and the Mg20Bi alloy anode is as follows: During discharge, the high-potential Mg_3Bi_2 phase discharges first, allowing Mg^{2+} to diffuse into the electrolyte. The remaining highly reactive Bi and Mg from the anode react with the MBN electrolyte, forming a solid electrolyte interphase (SEI), primarily on the α-Mg matrix. This leads to the formation of bubble-like structures due to surface tension. During charging,

Mg from the α-Mg phase preferentially desorbs and migrates into the MBN electrolyte, reversing the discharge process.

Figure 4A-C depicts the surface morphology of the Mg20Bi alloy cycled with MBN-Br at different times. At the initial cycle time, the surface of the alloy shows some dependent bubble-like grains with a surface area of 6 μm² (feature size: 3 μm), increasing to 150 μm² (feature size: 115 μm) at 200 h. Surprisingly, at the same time, the "bubbles" break, which may be attributed to the etching effect of Br^-[19]. When the cycle time is increased to 600 h, the bubble-like grains on the surface disappear and a two-phase structure with features measuring up to 3,000 μm² (feature size: 60 μm) in surface area is observed. In Figure 4C, corrosion pits are visible in the Mg matrix [Supplementary Figure 6], accompanied by Br accumulation [Figure 4D], suggesting that Br^- ions contribute to the etching process, which aligns with the proposed mechanism.

Additionally, EDS mapping of the Mg20Bi alloy anode cycled for 50 and 200 h [Supplementary Figure 7] shows Br concentrated at the edges of the broken bubble-like grains, indicating the presence of electrolytes, while Mg is more concentrated in the center of these grains.

Ex situ Mg 2*p* and Bi 4*f* XPS spectra of Mg20Bi alloy anodes are shown in Figure 4E. The Mg 2*p* spectra at 0 s only show the Mg^{II} state, assigned to 50.3 eV, while after 150 s, the metallic state of Mg^0 is observed at 48.2 eV. Meanwhile, the Bi^0 and Bi^{III} are found in the all etching Bi 4*f* spectra, indicating the presence of the metallic states in alloys and newly formed intermetallic states after electrochemical cycling times. Notably, the Bi^{III} binding energy for Bi $4f_{5/2}$ is 162.8 eV at 0 s, which is higher than 161.6 eV at 300 s and 161.5 eV at 150 s, indicating the insertion of Mg^{2+}, consistent with the insertion of Li^+[36] and Mg^{2+}[37]. Similarly, as shown in Supplementary Figure 8, the binding energy of Bi 4*f* spectra of Mg20Bi alloy anode cycling after 50 h and 200 h at 0 s is higher than at 150 s and 300 s. These strong shifts in the binding energy of Bi 4*f* indicate the process of Mg ion insertion into the Mg_3Bi_2 phase.

We compared the variations in Bi^{III} proportion in the Mg20Bi alloy at different cycling and etching times, as shown in Figure 4F. When the cycling time is at 50 h, Bi^{III} proportion decreases from 60% at 0 s to 15% at 150 s and 300 s, consistent with the formation of bubble-like SEI as in MBN. A similar trend is observed after cycling for 200 h, with a decrease from 53% at 0 s to 49% at 150 s and 300 s, accompanied by a significant overall decrease in Bi^{III} proportion, corresponding to the broken of the bubble-like SEI. Finally, when the cycling time was further increased to 600 h, the Bi^{III} proportion is uniformly distributed with 42% at 0 s and 45% at 150 s and 300 s, indicating the deeply uniform Mg stripping/plating process on the Mg20Bi alloy anode.

To compare the magnesiophilicity of Mg20Bi alloys, the interaction between the Mg atom and Mg/Mg_3Bi_2 phase surface was investigated by DFT calculations. Figure 5A illustrates the optimized configurations of Mg atoms adsorbed on the surface of Mg (101) and Mg_3Bi_2 (011) at different positions. There are different adsorption sites on the $Mg\text{-}Mg_3Bi_2$ surfaces, and the E_{ads} is much more negative at the top of Bi atoms (-0.48 eV) than at the top of Mg atoms (-0.18 eV), respectively, suggesting that the Bi atoms are the more Mg-friendly portion of the Mg_3Bi_2 phase. At the center of the rhombic tetrahedron formed by Mg and Bi atoms, the E_{ads} reaches -1.16 eV, which is much larger than the other two sites, indicating that Mg atoms tend to adsorb at this site on the surface of the Mg_3Bi_2 phase. The E_{ads} of Mg atoms on the Mg (101) surface is -0.75 eV, which is weaker than that on the Mg_3Bi_2 phase. Consequently, the Mg_3Bi_2 phase demonstrates a greater propensity for Mg atom adsorption compared to the Mg matrix phase, thereby effectively lowering the energy barrier for Mg^{2+} desolvation and subsequent nucleation on the anode surface.

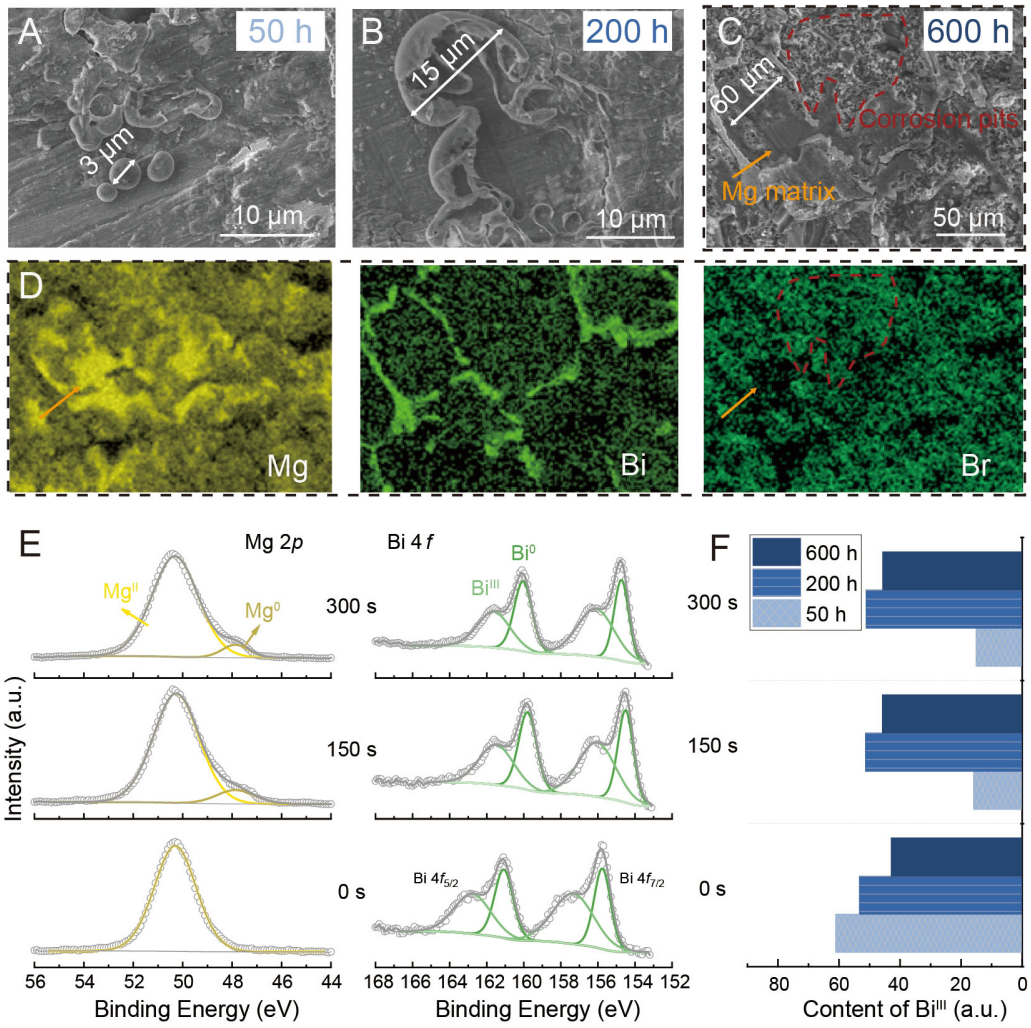

Figure 4. Mg20Bi alloy anode after cycling in Mg20Bi | MBN-Br | Mg20Bi symmetric cell. SEM of Mg20Bi alloy anode: (A) 50 h; (B) 200 h and (C) 600 h; (D) EDS mapping of Figure 4C; (E) XPS spectra at different etching times: Mg 2*p* and Bi 4*f* in Mg20Bi alloy anode after 600 h stripping/plating; (F) Variations in Bi^{III} proportion in the Mg20Bi alloy at different cycling and etching times. MBN-Br: $Mg(BH_4)_2{\cdot}1.9NH_3$-32 wt.% $MgBr_2{\cdot}2NH_3$; SEM: Scanning electron microscopy; EDS: Energy-dispersive X-ray spectrometer; XPS: X-ray photograph spectroscopy.

The diffusion energy barriers of Mg ions on the surfaces of Mg and Mg_3Bi_2 are also investigated. The calculated diffusion energy barriers for Mg ions on the Mg_3Bi_2 and Mg surfaces are 0.23 eV and 0.37 eV, respectively, as illustrated in Figure 5B and C. These results agree with the experimental observations discussed earlier. In comparison to the bare Mg phase, the Mg_3Bi_2 phase facilitates faster migration of Mg^{2+} ions. Additionally, the high affinity for Mg^{2+} and the rapid Mg^{2+} diffusion of the Mg_3Bi_2 phase effectively enhance the uniform flux of Mg^{2+} and promote the smooth deposition of Mg[25,38].

Mg metal anodes are of interest due to their susceptibility to passivation and poor compatibility with electrolytes. In conventional organic non-aqueous electrolytes, such as those containing ClO_4^-, PF_6^-, and BF_4^-, or reducing substances such as oxygen and water, localized electrochemical reactions often occur on the Mg metal surface. These reactions lead to the formation of hemispherical SEI due to inhomogeneous deposition at high current densities (e.g., 0.1 mA cm^{-2})[39-41]. These hemispherical SEIs generate a high

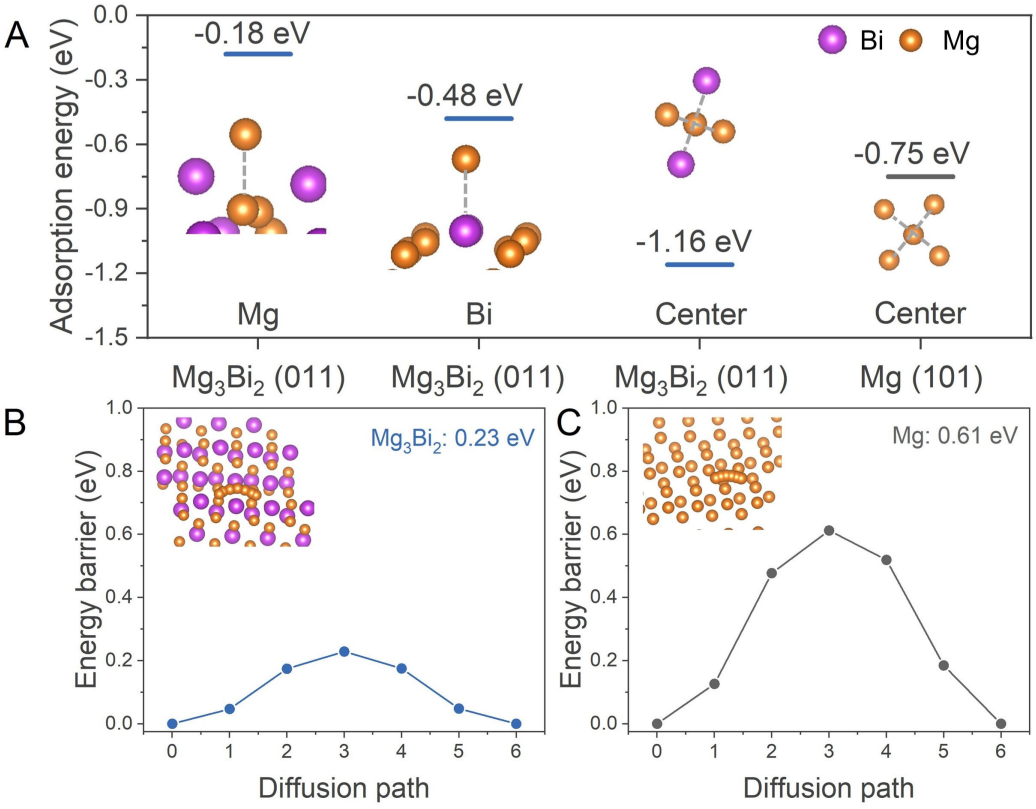

Figure 5. The interaction between Mg atom and the Mg/Mg_3Bi_2 phase surface. (A) Adsorption configurations and the corresponding adsorption energies of a Mg atom on the surfaces of Mg (101) and Mg_3Bi_2 (011); (B-C) The calculated Mg migration energy barriers in Mg_3Bi_2 (011) and Mg (101), respectively. Here, the orange and purple balls represent the Mg and Bi elements, respectively.

electric field around them, further accelerating the passivation of the interface. Furthermore, the incomplete deposition and dissolution efficiency of Mg, passivated by $TFSI^-$, Cl^-, and trace amounts of H_2O, leads to a net loss of metallic Mg. This results in the formation of irregular, porous, and friable morphologies[40]. Additionally, a layered SEI was found on the Mg anode with $Mg(BH_4)_2{\cdot}1.9NH_3$, and $MgBr_2{\cdot}2NH_3$ was introduced to enhance interface stability with the Mg anode. However, the formation mechanism remains unclear.

In the present study, the strategy and possible formation mechanism of the Mg stripping/plating process on MgBi alloy anodes with $Mg(BH_4)_2{\cdot}1.9NH_3$ and $Mg(BH_4)_2{\cdot}1.9NH_3$-$MgBr_2{\cdot}2NH_3$ are summarized in Figure 6, each illustrated in four distinct stages. At the initial stage (Stage I), Mg^{2+} ions directly electro-dissolute from the MgBi alloy anode in the absence of the passive SEI. The stripping potential ($E_{stripping}$) is mainly determined by the charge-transfer process (E_{ct}), with the values of 0.18 V for $Mg(BH_4)_2{\cdot}1.9NH_3$ and 0.05 V for $Mg(BH_4)_2{\cdot}1.9NH_3$-$MgBr_2{\cdot}2NH_3$, respectively [Figure 2A]. During the subsequent plating process, the high affinity of Mg^{2+} and the rapid diffusion of Mg^{2+} within the Mg_3Bi_2 phase significantly enhance the homogeneous fluxes of Mg^{2+}, promoting the fast kinetics of Mg deposition on the Mg_3Bi_2 phase [Figure 5]. As a result, the tiny passive bubble-like SEI will form on the surface of MgBi foil (Stage II). In this stage, the $E_{stripping}$ slightly increases due to the added ionic diffusion through interphases (E_{int})[42], resulting in the increase of impedance [Figure 2B and C].

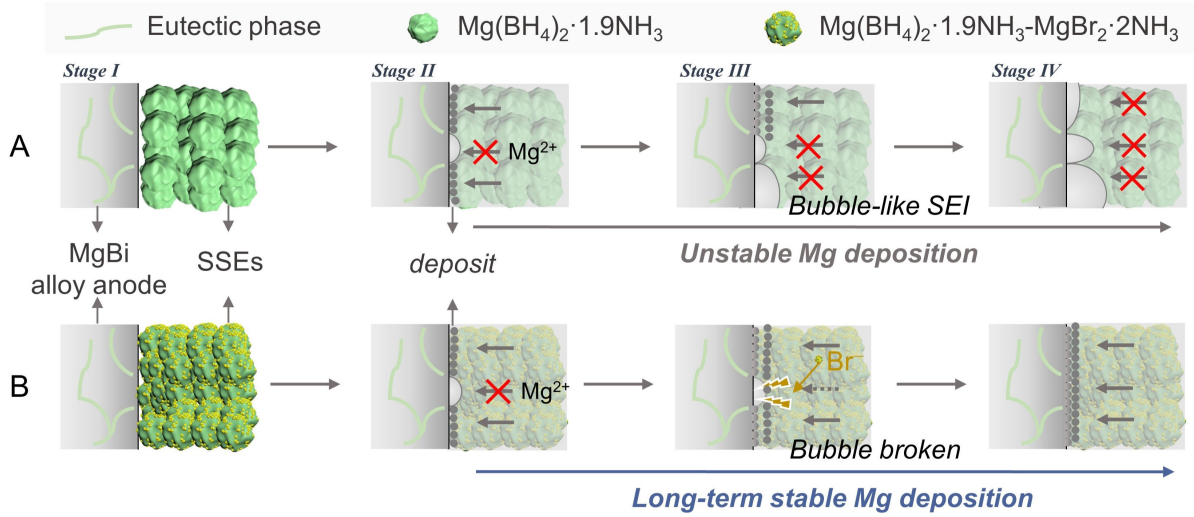

Figure 6. Schematic diagram of SEI evolution and Mg deposition behavior for (A) $Mg(BH_4)_2·1.9NH_3$ and (B) $Mg(BH_4)_2·1.9NH_3$-$MgBr_2·2NH_3$ on the MgBi alloy anode. SEI: Solid electrolyte interphase.

This bubble-like SEI, similar to "hot spots" on Mg foil at high current densities[43], expands and increases over cycling time, leading to a nonuniform Mg deposit on the anode (Stage III in Figure 6A). As a result, $E_{stripping}$ increases, and an unstable Mg stripping/plating process is exhibited (Stage IV in Figure 6A). In contrast, the presence of $MgBr_2·NH_3$ nanoparticles suppresses the formation of the bubble-like SEI (Figure 4 and Stage III in Figure 6B), attributing to the etching effect of Br^- ions, as evidenced in liquid electrolyte[19]. Once the bubble is broken, the deposition of Mg on the alloy anode becomes more uniform, leading to a long-term stable Mg stripping/plating process (Stage IV in Figure 6B).

CONCLUSION

We have investigated the Mg20Bi alloy as an anode for MIBs, focusing on its interfacial stability with solid state electrolytes (SSEs). Bubble-like SEI is formed between the MgBi alloy and $Mg(BH_4)_2·1.9NH_3$ SSE leading to unstable Mg stripping/plating, originating from remarkably different Mg deposition kinetics on the eutectic region (e.g., Mg + Mg_3Bi_2 phases) and on the Mg matrix. The decoration with $MgBr_2·2NH_3$ nanoparticles in $Mg(BH_4)_2·1.9NH_3$ SSE suppresses this bubble-like SEI through the etching effect of Br^-. Consequently, the interfacial stability between MgBi alloys and SSEs is notably improved, which allows the long-term stable stripping/plating for over 600 h at 0.1 mA cm^{-2} with a low overpotential of around 0.05 V.

DECLARATIONS

Authors' contributions

Investigation, DFT calculation, writing - original draft: Wang, Q.
Software supervision, writing - review and editing: Li, H.
Material characterization: Xu, T.
Supervision, funding acquisition, writing - review and editing: Yan, Y.
Supervision: Chen, Y.

Availability of data and materials

The data that support the findings of this study are available from the corresponding author upon reasonable request.

Financial support and sponsorship

This work was financially supported by the National Natural Science Foundation of China (No. 21975168). The authors appreciate Dr. Zhu, Y. for his assistance with SEM measurement. The authors would like to thank Shiyanjia Lab (www.shiyanjia.com) for the XPS tests. Wang, Q. acknowledges the financial support from the China Scholarship Council (202306240092). Li, H. acknowledges the Center for Computational Materials Science, Institute for Materials Research, Tohoku University for the use of MASAMUNE-IMR (No. 202312-SCKXX-0203), and the Institute for Solid State Physics (ISSP) at the University of Tokyo for the computational resources.

Conflicts of interest

All authors declared that there are no conflicts of interest.

Ethical approval and consent to participate

Not applicable.

Consent for publication

Not applicable.

REFERENCES

1. Zhao, Q.; Stalin, S.; Zhao, C.; Archer, L. A. Designing solid-state electrolytes for safe, energy-dense batteries. *Nat. Rev. Mater.* **2020**, *5*, 229-52. DOI
2. Unemoto, A.; Matsuo, M.; Orimo, S. Complex hydrides for electrochemical energy storage. *Adv. Funct. Mater.* **2014**, *24*, 2267-79. DOI
3. Higashi, S.; Miwa, K.; Aoki, M.; Takechi, K. A novel inorganic solid state ion conductor for rechargeable Mg batteries. *Chem. Commun.* **2014**, *50*, 1320-2. DOI PubMed
4. Ruyet R, Berthelot R, Salager E, Florian P, Fleutot B, Janot R. Investigation of $Mg(BH_4)(NH_2)$-based composite materials with enhanced Mg^{2+} ionic conductivity. *J. Phys. Chem. C.* **2019**, *123*, 10756-63. DOI
5. Le, R. R.; Fleutot, B.; Berthelot, R.; et al. $Mg_3(BH_4)_4(NH_2)_2$ as inorganic solid electrolyte with high Mg^{2+} ionic conductivity. *ACS. Appl. Energy. Mater.* **2020**, *3*, 6093-7. DOI
6. Roedern, E.; Kühnel, R. S.; Remhof, A.; Battaglia, C. Magnesium ethylenediamine borohydride as solid-state electrolyte for magnesium batteries. *Sci. Rep.* **2017**, *7*, 46189. DOI PubMed PMC
7. Burankova, T.; Roedern, E.; Maniadaki, A. E.; et al. Dynamics of the coordination complexes in a solid-state Mg electrolyte. *J. Phys. Chem. Lett.* **2018**, *9*, 6450-5. DOI
8. Kisu, K.; Kim, S.; Inukai, M.; Oguchi, H.; Takagi, S.; Orimo, S. Magnesium borohydride ammonia borane as a magnesium ionic conductor. *ACS. Appl. Energy. Mater.* **2020**, *3*, 3174-9. DOI
9. Yan, Y.; Dononelli, W.; Jørgensen, M.; et al. The mechanism of Mg^{2+} conduction in ammine magnesium borohydride promoted by a neutral molecule. *Phys. Chem. Chem. Phys.* **2020**, *22*, 9204-9. DOI
10. Yan, Y.; Grinderslev, J. B.; Jørgensen, M.; Skov, L. N.; Skibsted, J.; Jensen, T. R. Ammine magnesium borohydride nanocomposites for all-solid-state magnesium batteries. *ACS. Appl. Energy. Mater.* **2020**, *3*, 9264-70. DOI
11. Yan, Y.; Grinderslev, J. B.; Burankova, T.; et al. Fast room-temperature Mg^{2+} conductivity in $Mg(BH_4)_2{\cdot}1.6NH_3$-Al_2O_3 nanocomposites. *J. Phys. Chem. Lett.* **2022**, *13*, 2211-6. DOI
12. Wang, Q.; Li, H.; Zhang, R.; et al. Oxygen vacancies boosted fast Mg^{2+} migration in solids at room temperature. *Energy. Storage. Mater.* **2022**, *51*, 630-7. DOI
13. Zhang, J.; Wang, W.; Chen, X.; Jin, J.; Yan, X.; Huang, J. Single-atom Ni supported on TiO_2 for catalyzing hydrogen storage in MgH_2. *J. Am. Chem. Soc.* **2024**, *146*, 10432-42. DOI
14. Liu, F.; Cao, G.; Ban, J.; et al. Recent advances based on Mg anodes and their interfacial modulation in Mg batteries. *J. Magnes. Alloys.* **2022**, *10*, 2699-716. DOI
15. Son, S. B.; Gao, T.; Harvey, S. P.; et al. An artificial interphase enables reversible magnesium chemistry in carbonate electrolytes. *Nat. Chem.* **2018**, *10*, 532-9. DOI
16. Tang, K.; Du, A.; Dong, S.; et al. A stable solid electrolyte interphase for magnesium metal anode evolved from a bulky anion lithium salt. *Adv. Mater.* **2020**, *32*, e1904987. DOI

17. Chinnadurai, D.; Lieu, W. Y.; Kumar, S.; Yang, G.; Li, Y.; Seh, Z. W. A passivation-free solid electrolyte interface regulated by magnesium bromide additive for highly reversible magnesium batteries. *Nano. Lett.* **2023**, *23*, 1564-72. DOI
18. Chen, T.; Sai, G. G.; Canepa, P. Ionic transport in potential coating materials for Mg batteries. *Chem. Mater.* **2019**, *31*, 8087-99. DOI
19. Hebié, S.; Ngo, H. P. K.; Leprêtre, J. C.; et al. Electrolyte based on easily synthesized, low cost triphenolate-borohydride salt for high performance $Mg(TFSI)_2$-glyme rechargeable magnesium batteries. *ACS. Appl. Mater. Interfaces.* **2017**, *9*, 28377-85. DOI
20. Wang, Q.; Li, Z.; Deng, H.; Chen, Y.; Yan, Y. Enhanced interface stability of ammine magnesium borohydride by in situ decoration of $MgBr_2 \cdot 2NH_3$ nanoparticles. *Chem. Commun.* **2023**, *59*, 6726-9. DOI
21. Xu, X.; Chao, D.; Chen, B.; et al. Revealing the magnesium-storage mechanism in mesoporous bismuth via spectroscopy and Ab-initio simulations. *Angew. Chem. Int. Ed. Engl.* **2020**, *59*, 21728-35. DOI
22. Chen, X.; Wei, S.; Tong, F.; Taylor, M. P.; Cao, P. Electrochemical performance of Mg-Sn alloy anodes for magnesium rechargeable battery. *Electrochimica. Acta.* **2021**, *398*, 139336. DOI
23. Ikhe, A. B.; Han, S. C.; Prabakar, S. J. R.; Park, W. B.; Sohn, K.; Pyo, M. $3Mg/Mg_2$ Sn anodes with unprecedented electrochemical performance towards viable magnesium-ion batteries. *J. Mater. Chem. A.* **2020**, *8*, 14277-86. DOI
24. Wang, L.; Welborn, S. S.; Kumar, H.; et al. High-rate and long cycle-life alloy-type magnesium-ion battery anode enabled through (de) magnesiation-induced near-room-temperature solid-liquid phase transformation. *Adv. Energy. Mater.* **2019**, *9*, 1902086. DOI
25. Chai, X.; Xie, H.; Zhang, T.; et al. Ternary Mg alloy-based artificial interphase enables high-performance rechargeable magnesium batteries. *Energy. Storage. Mater.* **2024**, *70*, 103460. DOI
26. Singh, N.; Arthur, T. S.; Ling, C.; Matsui, M.; Mizuno, F. A high energy-density tin anode for rechargeable magnesium-ion batteries. *Chem. Commun.* **2013**, *49*, 149-51. DOI PubMed
27. Kravchyk, K. V.; Piveteau, L.; Caputo, R.; et al. Colloidal bismuth nanocrystals as a model anode material for rechargeable Mg-ion batteries: atomistic and mesoscale insights. *ACS. Nano.* **2018**, *12*, 8297-307. DOI
28. Jung, S. C.; Han, Y. Fast magnesium ion transport in the Bi/Mg_3Bi_2 two-phase electrode. *J. Phys. Chem. C.* **2018**, *122*, 17643-9. DOI
29. Yaghoobnejad Asl, H.; Fu, J.; Kumar, H.; Welborn, S. S.; Shenoy, V. B.; Detsi, E. *In situ* dealloying of bulk Mg_2Sn in Mg-ion half cell as an effective route to nanostructured Sn for high performance Mg-ion battery anodes. *Chem. Mater.30*, 1815-24. DOI
30. Kresse, G.; Furthmüller, J. Efficient iterative schemes for *ab initio* total-energy calculations using a plane-wave basis set. *Phys. Rev. B.* **1996**, *54*, 11169-86. DOI
31. Perdew, J. P.; Burke, K.; Ernzerhof, M. Generalized gradient approximation made simple. *Phys. Rev. Lett.* **1996**, *77*, 3865-8. DOI PubMed
32. Kresse, G.; Joubert, D. From ultrasoft pseudopotentials to the projector augmented-wave method. *Phys. Rev. B.* **1999**, *59*, 1758-75. DOI
33. Monkhorst, H. J.; Pack, J. D. Special points for brillouin-zone integrations. *Phys. Rev. B.* **1976**, *13*, 5188-92. DOI
34. Henkelman, G.; Uberuaga, B. P.; Jónsson, H. A climbing image nudged elastic band method for finding saddle points and minimum energy paths. *J. Chem. Phys.* **2000**, *113*, 9901-4. DOI
35. Nayeb-hashemi, A. A.; Clark, J. B. The Bi-Mg (Bismuth-Magnesium) system. *Bull. Alloy. Phase. Diagrams.* **1985**, *6*, 528-33. DOI
36. Pradhan, B.; Dalui, A.; Paul, S.; Roy, D.; Acharya, S. Solution phase synthesis of large-area ultra-thin two dimensional layered Bi_2Se_3: role of Cu-intercalation and substitution. *Mater. Res. Express.* **2019**, *6*, 124005. DOI
37. Xu, X.; Ye, C.; Chao, D.; et al. Synchrotron X-ray spectroscopic investigations of in-situ-formed alloy anodes for magnesium batteries. *Adv. Mater.* **2022**, *34*, e2108688. DOI
38. Li, Y.; Yang, G.; Zhang, C.; et al. Grain-boundary-rich triphasic artificial hybrid interphase toward practical magnesium metal anodes. *Adv. Funct. Mater.* **2023**, *33*, 2210639. DOI
39. Ding, M. S.; Diemant, T.; Behm, R. J.; Passerini, S.; Giffin, G. A. Dendrite growth in Mg metal cells containing $Mg(TFSI)_2$/glyme electrolytes. *J. Electrochem. Soc.* **2018**, *165*, A1983-90. DOI
40. Yoo, H. D.; Han, S. D.; Bolotin, I. L.; et al. Degradation mechanisms of magnesium metal anodes in electrolytes based on $(CF_3SO_2)_2N^-$ at high current densities. *Langmuir* **2017**, *33*, 9398-406. DOI
41. Dewitt, S.; Hahn, N.; Zavadil, K.; Thornton, K. Computational examination of orientation-dependent morphological evolution during the electrodeposition and electrodissolution of magnesium. *J. Electrochem. Soc.* **2016**, *163*, A513-21. DOI
42. Zhang, Y.; Li, J.; Zhao, W.; et al. Defect-free metal-organic framework membrane for precise ion/solvent separation toward highly stable magnesium metal anode. *Adv. Mater.* **2022**, *34*, e2108114. DOI
43. Wan, B.; Dou, H.; Zhao, X.; et al. Three-dimensional magnesiophilic scaffolds for reduced passivation toward high-rate Mg metal anodes in a noncorrosive electrolyte. *ACS. Appl. Mater. Interfaces.* **2020**, *12*, 28298-305. DOI